

Humidity-enhanced NO₂ gas sensing using atomically sharp edges in multilayer MoS₂

Abhay V. Agrawal,[†] Alexander Yu. Polyakov,[†] Jens Eriksson,[‡] Tomasz J. Antosiewicz,^{¶,†} and Timur O. Shegai*,[†]

[†] *Department of Physics, Chalmers University of Technology, 412 96 Göteborg, Sweden*

[‡] *Department of Physics, Linköping University, 581 83 Linköping, Sweden*

[¶] *Faculty of Physics, University of Warsaw, Pasteura 5, 02-093 Warsaw, Poland*

E-mail: timurs@chalmers.se

Abstract

Ambient humidity poses a significant challenge in the development of practical room temperature NO₂ gas sensors. Here, we employ atomically precise zigzag edges in multilayer MoS₂, fabricated using electron beam lithography and anisotropic wet etching, to achieve highly sensitive and selective gas sensing performance that is humidity-tolerant at elevated temperatures and humidity-enhanced at room temperature under ultraviolet illumination. Notably, exposure to 2.5 parts per billion (ppb) NO₂ at 70% relative humidity under ultraviolet illumination and at room temperature resulted in a 33-fold increase in response and a 6-fold faster recovery compared to 0% relative humidity, leading to response values exceeding 1100%. The optimized samples demonstrated a theoretical detection limit ranging from 4 to 400 parts per trillion (ppt) NO₂. The enhanced NO₂ sensing capabilities of MoS₂ edges have been further confirmed through first-principles calculations. Our study expands the applications of nanostructured MoS₂ and highlights its potential for detecting NO₂ at sub-ppb levels in complex scenarios, such as high humidity conditions.

Introduction

Detecting NO_2 is crucial in modern society, as it is a common industrial byproduct of any high-temperature combustion in nitrogen containing environments.^{1,2} NO_2 interacts with water and volatile organic compounds (VOCs) to contribute to the formation of acid rain and photochemical smog. Prolonged exposure to even low concentrations, such as 1 part per million (ppm) of NO_2 , can lead to the development of chronic bronchitis, respiratory-related diseases, and ocular discomfort.^{2,3} Furthermore, NO_2 is extensively used in the production of nitric acid, a substance that finds a widespread use.⁴ A pulmonary condition, known as asthma, is often associated with elevated levels of nitric oxides (NO_2 and NO) in the exhaled breath. While the exhaled nitric oxide (NO) concentration typically ranges from 20 to 25 parts per billion (ppb) in healthy individuals, those with asthma exhibit elevated levels ranging from 35 to 50 ppb, regardless of age.⁵ Recognizing these health risks, the United States Environmental Protection Agency (U.S. EPA) has set a regulated limit for exposure to NO_2 at 53 ppb.⁶ Consequently, there is a pressing need for reliable sensors capable of detecting minute concentrations of NO_2 below the regulatory threshold.^{6,7}

Various methods have been employed to detect NO_2 at ppb levels using MoS_2 . MoS_2 is a semiconducting material exhibiting a thickness-dependent bandgap (1.2-1.8 eV), high surface-to-volume ratio, a wide spectrum of light absorption from ultraviolet (UV) to near-infrared (near-IR), as well as excellent catalytic and gas sensing properties.⁸⁻¹⁰ Edges of MoS_2 have attracted research interest as favorable sites for gas adsorption, surpassing their basal plane counterparts. This phenomenon stems from the existence of vacancies (and other defects) supporting high binding energies and charge transfer values for target gas molecules.¹¹⁻¹³ It has been observed both theoretically and experimentally that the adsorption of NO_2 molecules is favorable at MoS_2 edges in comparison to other gases such as H_2 , CO , NH_3 , H_2S , CO_2 , and CH_4 .¹¹⁻¹³ Various advanced methods for improved gas sensing using MoS_2 include decoration of the latter with metal nanoparticles (NPs), fabricating van der Waals heterostructures, and morphology engineering. For example, Kim *et al.* functionalized

a solution-based MoS₂ surface with different noble metal NPs.¹⁴ The selective character of MoS₂ sensors may be modified by doping with metal NPs in order to target a specific gas. Long *et al.* proposed a MoS₂/graphene heterostructure for ultrasensitive NO₂ detection. At room temperature (RT), this hybrid structure demonstrated a 50 ppb NO₂ detection.¹⁵ A notable advantage of MoS₂ heterostructures is their rapid charge separation, which has the potential to develop gas sensors with fast response and recovery times. Although these strategies could pave the way to developing ultra-sensitive and selective NO₂ sensors, both methods introduce fabrication complexity in device manufacturing. Furthermore, the use of noble metal NPs is potentially costly.

Recently, gas sensors based on edge-enriched MoS₂ have emerged as a promising prospect. Edge-enriched MoS₂ offers a higher surface area and more active edge sites. Real-world devices and applications such as transistors, catalysts, photodetectors, and gas sensors based on nanopatterned transition metal dichalcogenides (TMDs), especially MoS₂, can experience significant improvements in their properties through edge enrichment.^{12,16–20} Cho *et al.* compared gas adsorption on three distinct morphologies of MoS₂ (horizontally aligned (HA) MoS₂, vertically aligned (VA) MoS₂ and a mixture of HA and VA MoS₂) grown by the combination of radio frequency (RF) sputtering and rapid sulfurization.¹² The authors showed theoretically that zigzag edges in MoS₂ provide an 18 times higher binding energy for NO₂ molecules adsorption compared to the basal plane. The experimental and theoretical investigations indicated that edge-enriched MoS₂ has a superior sensitivity for NO₂ gas molecules. Agrawal *et al.* proposed chemical vapor deposition (CVD) grown mixed in-plane and edge-enriched MoS₂ flakes.¹³ The proposed structures showed a selective and sensitive nature for NO₂ sensing at room temperature. Li *et al.* used the hydrothermal method to prepare hollow, solid, and smooth MoS₂ nanospheres. The sensing area for NO₂ was doubled, and the response was enhanced 3.1 times in hollow MoS₂ in comparison to smooth nanospheres. Edges in MoS₂ can be either zigzag or armchair, among which the zigzag edges are thermodynamically more stable and most promising for gas molecule adsorption.²¹ How-

ever, in most morphology-driven NO₂ sensors, it is challenging to accurately control the precise edge orientation.

The top-down nanopatterning can substantially modify the structural, optical, and electrical characteristics TMDs materials. These properties are strongly influenced by changes in the atomic-scale structure and defects.^{20,22,23} Numerous methods, such as atomic force lithography, plasma treatment, block copolymer lithography (BCP), thermal annealing, laser writing, and seed-assisted growth, have been used previously.²⁴⁻²⁹ However, these approaches lead to reduced accuracy and sharpness, random orientation, uneven patterning, complex fabrication stages, and limited control over the size and shape of the nanostructures. In seed-assisted patterning, for instance, the resulting TMD materials may exhibit random orientation and face a continuous risk of contamination from seeds throughout the growth process.^{28,30} The laser writing and thermal annealing methods potentially eliminate the necessity for masks and photoresists, simplifying the nanopattern design.^{31,32} Similarly, BCP lithography has emerged as a promising strategy for nanopatterning. However, in all these processes, the patterns are typically randomly orientated, not precisely controlled, disordered, and contain structural defects.¹⁹

In addition to the aforementioned challenges, it is important to recognize that the relative humidity (RH) commonly present in the atmosphere poses a significant obstacle to the development of real-time gas sensors using semiconducting materials. The water concentration in ambient air (atmospheric pressure, 25°C) is 6,280 ppm at 20% RH and 25,740 ppm at 80% RH levels, respectively.³³ Moreover, in real-life scenarios, the humidity levels are strongly dependent on environmental conditions, such as wind, rainfall, temperature, as well as day-night and seasonal oscillations. At room temperature, water adsorption leads to significant fluctuations in baseline resistance with variations in humidity.³⁴⁻³⁶ Additionally, exhaled human breath contains substantial RH levels, which presents a challenge for reliable chemiresistive gas sensor operation. A commonly employed approach to overcome these challenges is elevated temperatures. Furthermore, various approaches to develop humidity-

tolerant chemiresistive gas sensors, such as doping with metal NPs (Pd, Pt, Ag, Au), element doping (Ce, Pr, and Tb), integration with hydrophobic materials (polydimethylsiloxane (PDMS), prepared polyaniline (PANI), graphite nanoflakes) *etc.* have been previously employed.^{33,37–43} Although such methods improved the anti-humidity ability of the respective gas sensors, each mentioned approach added complexity, hindering their practical use.

Here, we report sub-ppb-level NO₂ sensors based on nanopatterned multilayer MoS₂ exposing precise atomically sharp zigzag edges. The nanopatterned MoS₂ resulted in honeycomb nanomesh structures fabricated by optimizing the process reported earlier.²² The method provides a uniform, precise, and controllable mesh of MoS₂ nanoribbons with widths ranging from a few hundred nanometers (nm) to sub ten nm (see Figure 1b-d). We studied the concentrations of NO₂ gas in the range of 2.5 – 10 ppb, below the threshold limit set by the U.S. EPA. The density of exposed edges is proportional to the hexagonal holes' density and their dimensions. We systematically studied the density-dependent NO₂ sensing in several honeycomb MoS₂ nanomesh samples. The NO₂ response was best at 200°C in the optimized honeycomb MoS₂ nanomesh structures due to numerous exposed, uniform, precise zigzag edges, combined with optimal electrical performance. The studied samples demonstrated selective NO₂ sensing (against CO, CH₄, H₂, and C₂H₆) and demonstrated an extraordinary limit of detection ranging from 4 to 400 ppt, depending on the exact mode of operation. In addition, we investigated the room temperature operation of our sensors under high RH levels (up to 70%) with and without UV illumination. Surprisingly, at RT the sensors showed a significantly enhanced response to NO₂ in a high-humidity environment. Under UV illumination, this humidity-enhanced response exceeds 1100% upon exposure to 2.5 ppb NO₂. Importantly, the humidity-enhanced sensing behavior is universal and was observed for other tested gases, including CO, CH₄, H₂, and C₂H₆, albeit at much lower response levels than for NO₂. This universal humidity-enhanced behavior suggests that the mechanism of the enhanced sensor performance is also universal, and likely involves competition between H₂O and O₂ adsorbed on the MoS₂ surface under the influence of UV illumination.

Our density functional theory (DFT) calculations confirm that NO_2 adsorption is significantly influenced by the presence of edges and sulfur vacancies. Thus, the honeycomb MoS_2 nanomesh samples, studied here, offer an optimal configuration, featuring a high density of sulfur vacancy sites along the multilayer hexagon rims. This unique structure enhances the NO_2 adsorption capacity, making the honeycomb MoS_2 nanomesh particularly effective for chemiresistive gas sensing applications in high humidity conditions.

Results and discussion

Nanofabrication, morphology, and structure of honeycomb MoS_2 nanomesh sensors

Figure 1 illustrates the fabrication process for honeycomb MoS_2 nanomeshes in multilayer MoS_2 . A comprehensive exploration of the fabrication process is presented in the experimental section and elsewhere.²² Using this method, we obtain hexagonal holes with atomically sharp zigzag edges. The scanning electron microscope (SEM) images of highly precise, uniform and large-area honeycomb MoS_2 nanomeshes formed by numerous holes are shown in Figure 1b-d. The center-to-center distance (pitch) between the two neighboring circles (defined by electron beam lithography (EBL) and dry etching) was kept fixed at 400 nm while the circle's radius varied from 280 to 300 nm in steps of 10 nm. The nano-ribbons achieved by this unique method are down to sub-ten-nanometer width with ultrahigh precision, as depicted in Figure 1b-d.

A similar set of honeycomb MoS_2 nanomeshes was prepared for the chemiresistive gas sensing assessment. The SEM images of the fabricated sensing devices are shown in Figure 2a-d. We designed the different testing devices on the same multilayer flake (30-40 nm thickness determined by profilometer) to minimize potential variations in electrical signal that may occur due to thickness, local defects, and fabrication processes and ensure a reliable comparison. In total, we fabricated four devices with channel lengths of 20 μm and

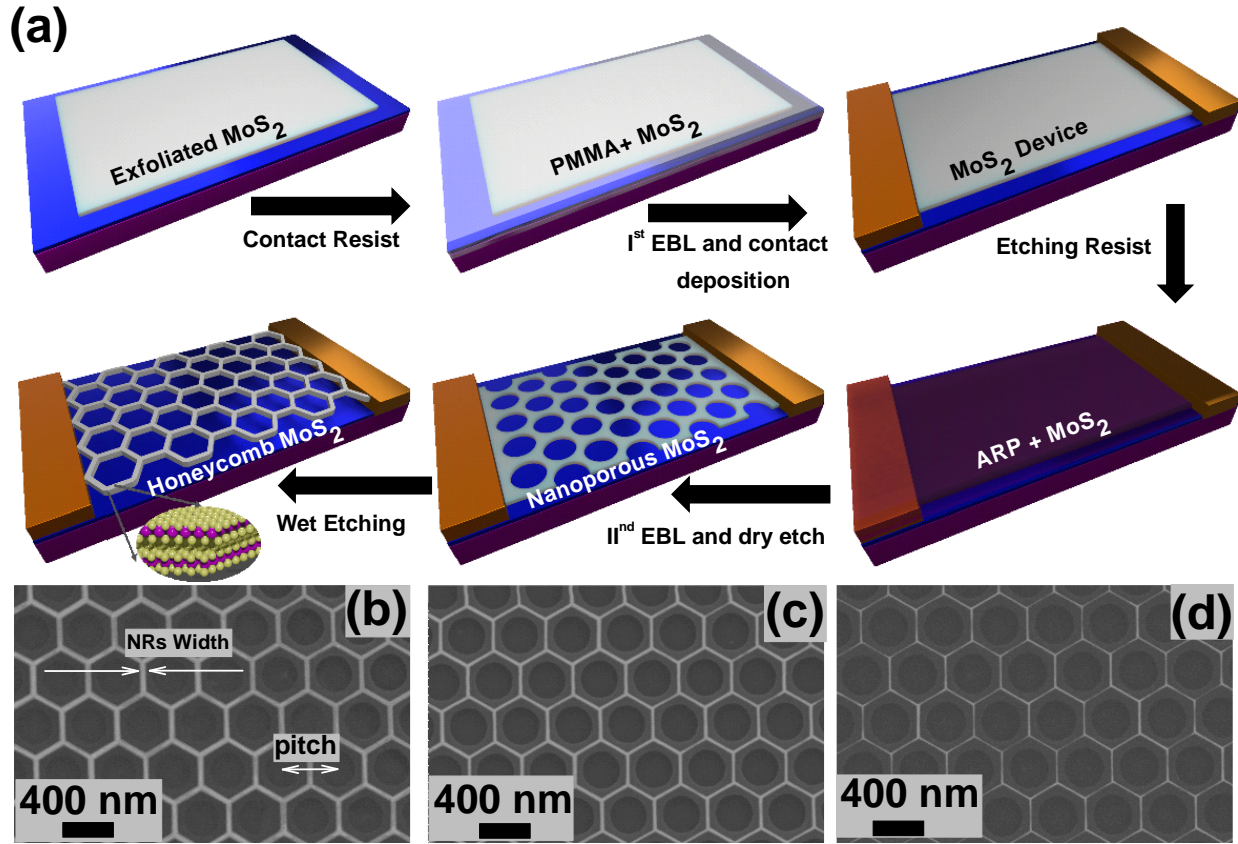


Figure 1: (a) Schematic illustration of the fabrication process towards honeycomb MoS₂ nanomeshes. (b-d) The SEM images of deterministically nanofabricated, highly uniform, and controlled honeycomb nanomeshes with precise zigzag edges. The nanomeshes are formed by triangular arrays of holes with fixed pitch 400 nm and variable radius of the initial circular holes (b) 280 nm (c) 290 nm (d) 300 nm.

widths of 13 μm , each. Among these four devices, three contain various honeycomb MoS₂ nanomeshes, while one remains unpatterned. The nomenclature for the fabricated devices is as follows: the unpatterned device is labeled as H0, while the patterned devices are denoted as H1, H2, and H3. To test the density-dependent NO₂ sensing, the initial size of the circles was varied. The density-dependent honeycomb meshes of H1, H2, and H3 devices were generated from the initial circular holes of 450, 250, and 100 nm radii, with nanomesh pitches – 1450, 820, and 325 nm, respectively. The low-magnification SEM images of the devices are shown in Figure 2a-d and illustrate precise, clean, and ultra-sharp fabrication of honeycomb MoS₂ nanomeshes with numerous zigzag edge sites available at the rims of hexagonal

holes. Step-by-step optical images illustrating the nanofabrication process, starting from exfoliation and ending with honeycomb MoS₂ nanopatterning are shown in the Supporting Information (SI), Figure S1. The SEM and optical images illustrate that the fabrication process does not damage MoS₂ the remaining areas of the flake or leave photoresist residues on the sensing elements. The sensor chip mounted on the Pt100 heater with a Transistor Outline (TO8) header is shown in Figure S1e. The header with a sensor chip was installed inside our home-built sensing chamber and subsequently used for gas sensing experiments.

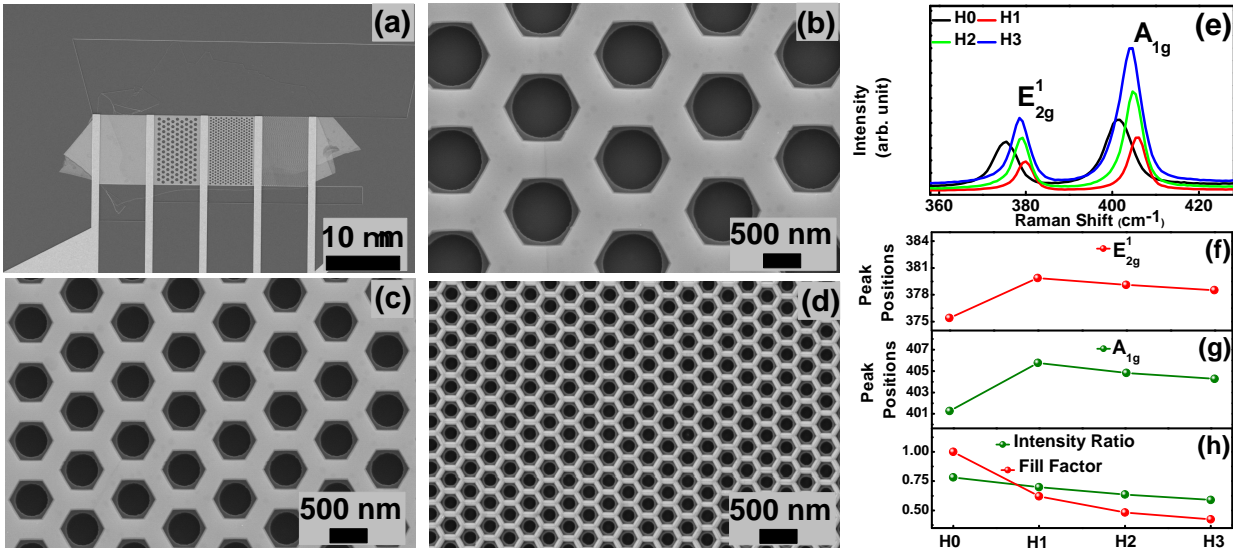


Figure 2: (a) The SEM image of tested devices. The high magnification SEM images of variable size hexagons (b) $R = 450$ nm and pitch – 1450 nm. (c) $R = 250$ nm and pitch – 820 nm. (d) $R = 100$ nm and pitch – 325 nm. (e) The Raman spectra of various patterned devices. Variation in peak position as a function of various size hexagons (f) E_{2g}^1 . (g) A_{1g} . (h) The change in Intensity ratio (E_{2g}^1/A_{1g}) with various size hexagons (blue). The calculated fill factor of each device (red)

The precise zigzag nature of hexagon MoS₂ was confirmed previously in detail using high-resolution transmission electron microscopy (HR-TEM).²² Here, we performed the Raman spectroscopy on patterned devices (H1, H2, and H3) and unpatterned device H0. Raman spectroscopy serves as a powerful and non-destructive technique, enabling the study of film orientation, doping, and the number of layers.^{44–46} Two distinct Raman modes, corresponding to the in-plane vibrations (E_{2g}^1) and out-of-plane vibrations (A_{1g}) of S and Mo atoms,

have been observed, as depicted in Figure 2e. Both E_{2g}^1 and A_{1g} peaks exhibit a blue shift upon nanopatterning compared to the unpatterned device, see Figure 2f-g. The A_{1g} peak is sensitive to changes in electron concentration and the blue shift in A_{1g} could signal a p -type doping in patterned devices.^{44,45} A more comprehensive discussion of p -doping observed through electrical measurements is provided in subsequent sections. However, we also observe that both Raman peaks exhibit a slight redshift with increasing hexagon density (devices from H1 to H3). The redshift in the E_{2g}^1 and A_{1g} modes can be attributed to terrace-terminated defects and an increase in MoS_2 edge density.^{46,47} The difference between the E_{2g}^1 and A_{1g} peak positions, which is sensitive to the material thickness, is around 25 cm^{-1} for all devices, implying the preservation of the device thicknesses with etching. E_{2g}^1 and A_{1g} modes correspond to in-plane and out-of-plane vibrations, respectively. Thus, the peak intensity ratio of (E_{2g}^1/A_{1g}) can be used to identify the exposed edges in MoS_2 .⁴⁸ In our case, the peak intensity ratio is also decreased from 0.78 to 0.58 (in an H0 – H3 row), indicating a clear increase in the number of edges with nanopatterning.

To confirm the increase in MoS_2 edge content, we calculated the fill factor based on SEM images. The fill factor is defined as the ratio between the effective MoS_2 area of the device to the area of the unpatterned device. The calculated fill factor is 1, 0.62, 0.48, and 0.42 for devices H0, H1, H2, and H3, respectively. These values quantify the increase in the edge content with the increasing hexagon density, see Figure 2h. The Raman signal originating from A_{1g} mode or from edges is increased simultaneously with the decrease in fill factor.

NO_2 gas sensing

We now turn our attention to the gas-sensing performance of our devices. The NO_2 sensing experiments were conducted using synthetic air background (80% O_2 and 20% N_2). We tested four different concentrations of NO_2 , ranging from 2.5 to 10 ppb, at two different operating temperatures: 200°C and RT. The gas sensing performance was evaluated at a fixed bias voltage, $V_{bias} = +1 \text{ V}$, via two-probe resistance measurements for all four devices.

The initial current-voltage ($I - V$) analysis revealed a notable trend: an increase in p -doping levels correlated with the rise in hexagon density within the fabricated devices. Detailed $I - V$ characteristics are provided in Figure S2.

NO₂ sensing at 200°C

The NO₂ sensing response at 200°C without humidity is shown in Figure 3. Here, the response (R , measured in %) is defined as the ratio of change in the resistance upon exposure to NO₂ (R_{gas}) to the base resistance in synthetic air (R_{air}): $R(\%) = \left(\frac{R_{gas} - R_{air}}{R_{air}}\right) \times 100$. The NO₂ gas was injected for 600 s and then turned off to allow for recovery in the background environment for all measurements. The left axis of each graph displays the calculated variation in response, while the right axis shows the corresponding variation in resistance.

In Figure 3a-d, the baseline resistance is increased from 0.12 M Ω for the unpatterned device to 0.8 M Ω for H3. This is attributed to the concurrent rise in the p -doping effect due to the increased density of hexagonal holes in the honeycomb MoS₂ nanomeshes, as discussed in SI. The observed increase in resistance with NO₂ exposure suggests that NO₂ is acting as an electron acceptor from n -type MoS₂. Moreover, the change in resistance due to NO₂ exposure is also concurrently increasing with the density of honeycomb MoS₂ nanomeshes. The obtained response to 2.5 ppb NO₂ is 48%, 64%, 100% and 120% for devices H0, H1, H2, and H3, respectively. These results demonstrate that our devices are highly sensitive even to trace amounts of NO₂. The response value indicates fewer available NO₂ adsorption sites in the unpatterned device, whereas in the nanomeshes, these sites' density increases, as shown in Figure 3e. When the devices are exposed to NO₂, the NO₂ gas is accepting electrons from the n -type MoS₂ surface due to its strong oxidative nature.^{12,49} As the hexagonal hole density increases from device H1 to H3, the number of zigzag edge sites also increases. The zigzag edges have higher chemical activity and strong gas adsorption ability in comparison to MoS₂ basal plane (as we demonstrate in DFT section below). This makes them highly attractive sites for NO₂ adsorption.^{10,11} Another interesting outcome observed in Figure 3a-d

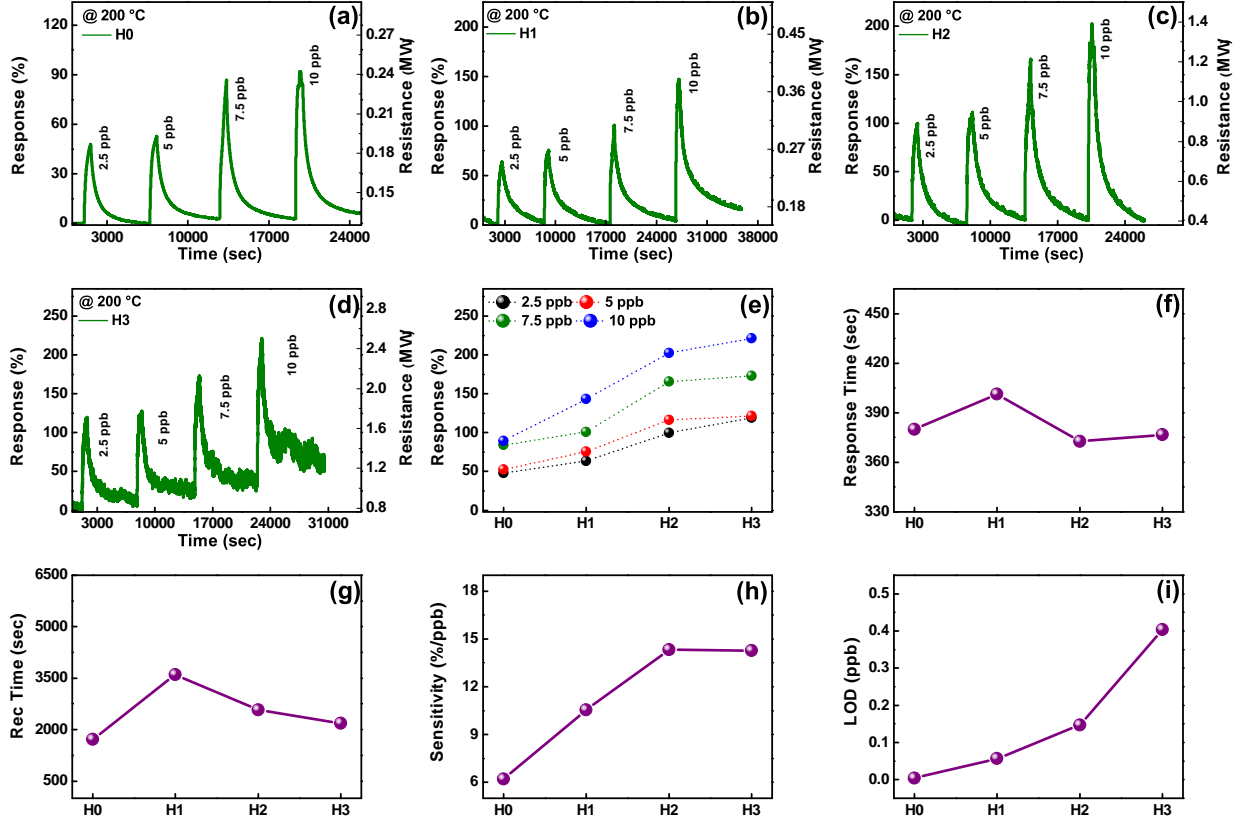


Figure 3: The dynamic NO₂ sensing response (2.5 – 10 ppb) at 200°C and 0% humidity obtained from (a) the unpatterned device (H0) and (b-d) honeycomb MoS₂ nanomeshes with the initial radius of circular holes: (b) R = 450 nm (H1). (c) R = 250 nm (H2). (d) R = 100 nm (H3). The calculated sensing parameters: (e) Summarized sensing response (%); (f) The response time (s) from each device calculated at 2.5 ppb NO₂ concentration; (g) The recovery time (s) from each device calculated from 2.5 ppb; (h) Sensitivity; (i) Limit of Detection (LOD).

is the increase in resistance noise in devices H0 to H3. The low signal-to-noise ratio poses an unavoidable obstacle in the trace detection of gases. Taking this into consideration, we have selected sensor device H2 as the optimal nanopatterned device, combining high sensitivity with low noise, and unpatterned device H0 as the control device for future optimization. Sensing parameters, including response (%), response time, and recovery time, are depicted in Figure 3e-g. The response time is determined by measuring the time interval between the sensor's transition from 10% to 90% of its response range. Similarly, the recovery time is characterized by the duration between the sensor's response shifting from 90% to 10% of its range. The response time ranges from 380 to 402 s, while recovery time falls in the

range of 1500 to 3600 s for a 2.5 ppb NO₂ cycle of each device. It is worth noting that the baseline resistance is nearly recovered to its initial level in synthetic air for each device at high operating temperatures, confirming the good recovery kinetics of each device. The sensitivity (S , measured in %/ppb) is also an important factor and it is given by the slope of response (%) and concentration (C_{NO_2} , ppb), $S = \frac{R(\%)}{C_{NO_2}}$.⁵⁰

The calculated sensitivity profile is shown in Figure 3h. It is evident that for the unpatterned device H0, the sensitivity is the lowest while reaching the highest values for the honeycomb MoS₂ nanomesh device H2, and saturating for device H3. The elevated sensitivity values imply a maximum change in response (%) can occur per ppb NO₂ exposure. Moving on, we calculated the limit of detection (LOD) for each device, as illustrated in Figure 3i. The LOD was calculated using the following equation: $LOD = \frac{3RMS_{noise}}{S}$, where S is the slope given by the response *vs.* concentration curve. The RMS_{noise} can be calculated using: $RMS_{noise} = \sqrt{\frac{\sum_{i=1}^N (R_i - \bar{R})^2}{N}}$. Additional details about fitting LOD data are provided in Figures S3-S4.

Remarkably, at 200°C, the unpatterned device H0 exhibited the lowest LOD of 4 ppt, although its sensitivity was the lowest. At the same time, a honeycomb nanomesh device H2 showed an impressive LOD of 400 ppt combined with exceptional sensitivity, a notable achievement compared to the state-of-the-art (comparison between various sensing platforms is discussed below). The low LOD of H0 can be attributed to the high signal-to-noise ratio in the unpatterned device compared to honeycomb patterned MoS₂ devices H1 – H3.

Humidity-tolerant and selective NO₂ sensing at 200°C

Humidity is a critical issue in developing gas sensor applications. Typically, the baseline resistance is greatly affected by the presence and variation in humidity levels. Thus, real-world gas sensors are difficult to obtain under variable humidity.^{51–53} Considering this, we have tested our sensors for the different RH levels, such as 0%, 30%, 50%, and 70%. The gas sensing performance for the unpatterned device H0 and honeycomb MoS₂ nanomesh device

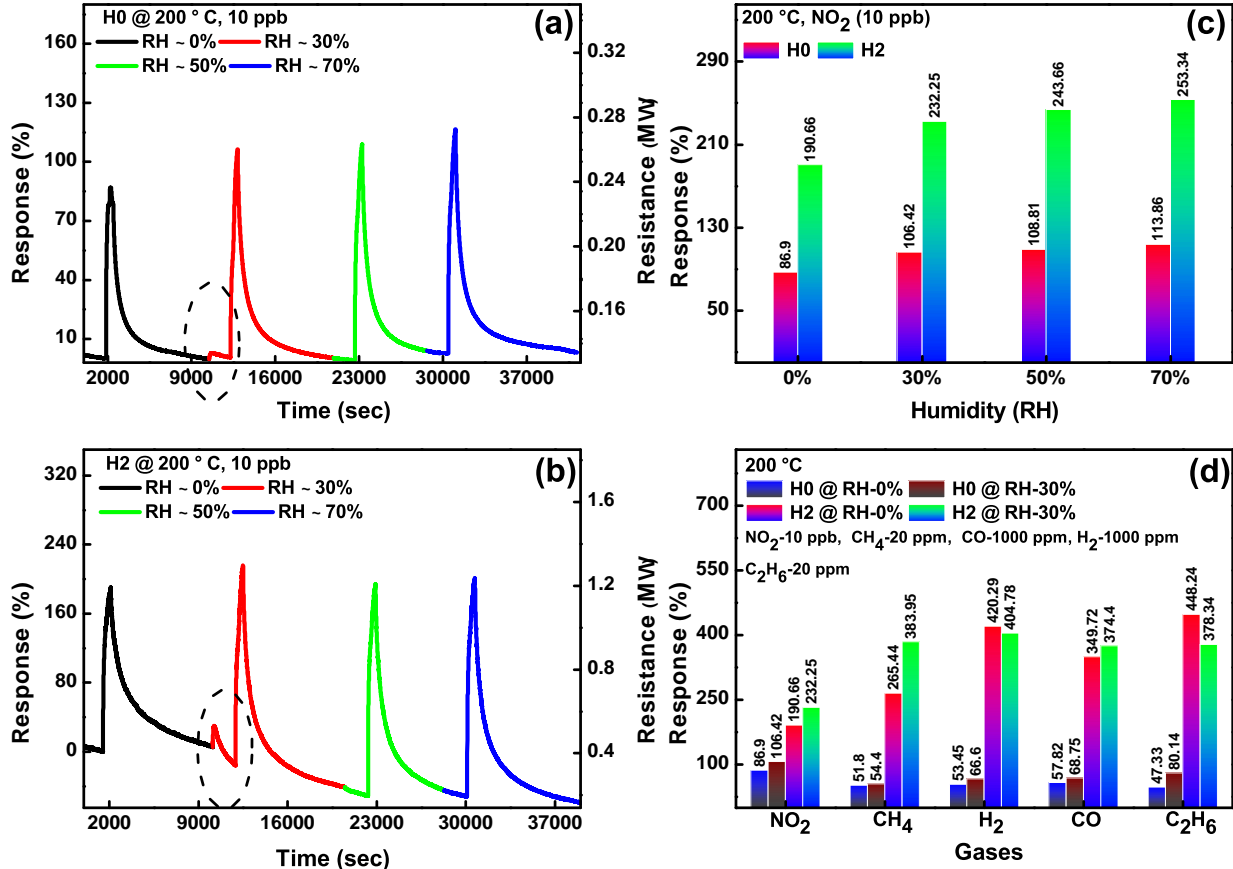


Figure 4: The dynamic NO₂ sensing for 10 ppb at 200°C for variable humidity ranging from 0% to 70% (a) Unpatterned device (H0). (b) Honeycomb MoS₂ nanomesh device (H2). (c) The comparative sensing response (%) for 10 ppb NO₂ for unpatterned device (H0) and honeycomb nanomesh device (H2). The selectivity profile for the unpatterned device and honeycomb nanomesh device (H2) under 0% and 30% humidity.

H2 at 10 ppb NO₂ and 200°C against variable humidity has been assessed. As depicted in Figure 4a-b, both devices remain almost unaffected by variations in humidity levels. Interestingly, we observed that both devices exhibited slightly enhanced NO₂ responses in the presence of humidity. When the 30% humidity was inserted in the chamber, there was a sudden rise in the response, shown as the dotted circle for both devices in Figure 4a-b. However, with a further increase in RH levels, we did not observe any substantial variations in baseline resistance. The unpatterned device H0 maintained a stable baseline, while the honeycomb nanomesh device H2 exhibited a gradual decrease in baseline resistance over the same period due to faster recovery under humidity (for additional details, see SI, Section

6.0.6).

A bar graph comparison of calculated response (%) for both devices is shown in Figure 4c. The honeycomb nanomesh device exhibited higher NO₂ sensing performance under different humidity variations. The detailed sensing mechanism of NO₂ interaction with unpatterned and honeycomb MoS₂ nanomeshes under a humid environment is discussed in detail later in the mechanism section in SI.

Selectivity is another important aspect of developing a versatile gas sensor. In Figure 4d, we present the selectivity experiments for different gases such as NO₂, CH₄, H₂, CO, C₂H₆ under the 0% and 30% humidity. The unpatterned device H0 showed nearly the same response for all mentioned gases. However, the nanopatterned device H2 showed exceptional selectivity for NO₂ under 0% and 30% humidity. Remarkably, the concentrations of other gases were in the 20 – 1000 ppm range, while NO₂ was present at the 10 ppb level. The difference between the responses therefore exceeds 1000 times in favor of NO₂. This confirms the selective nature of the honeycomb nanomesh devices for NO₂ gas sensing. Based on these results, we conclude that our devices are highly sensitive and selective towards trace detection of NO₂ even at high relative humidity levels (see Figure S5 for complete sensing cycles).

Room temperature NO₂ sensing under UV illumination: excellent recovery and humidity-enhanced response

An alternative to the heating approach to counteract the effects of moderate humidity levels is the material surface activation by UV light. UV activation is efficient in forcing desorption of O₂ and H₂O from MoS₂, which facilitates interactions of NO₂ with the material surface due to higher availability of adsorption sites.^{54,55} We performed NO₂ sensing experiments under continuous humidity exposure for a wide range of RH ranging from 0% to 70% (NO₂ sensing results at RT without UV illumination, i.e. in the dark, is discussed in detail in SI and Figure S6). The broad sensing profile is shown in Figure 5a. As previously, we used four NO₂ concentrations – 2.5, 5, 7.5, and 10 ppb, tested at each humidity level. The grey, green, blue,

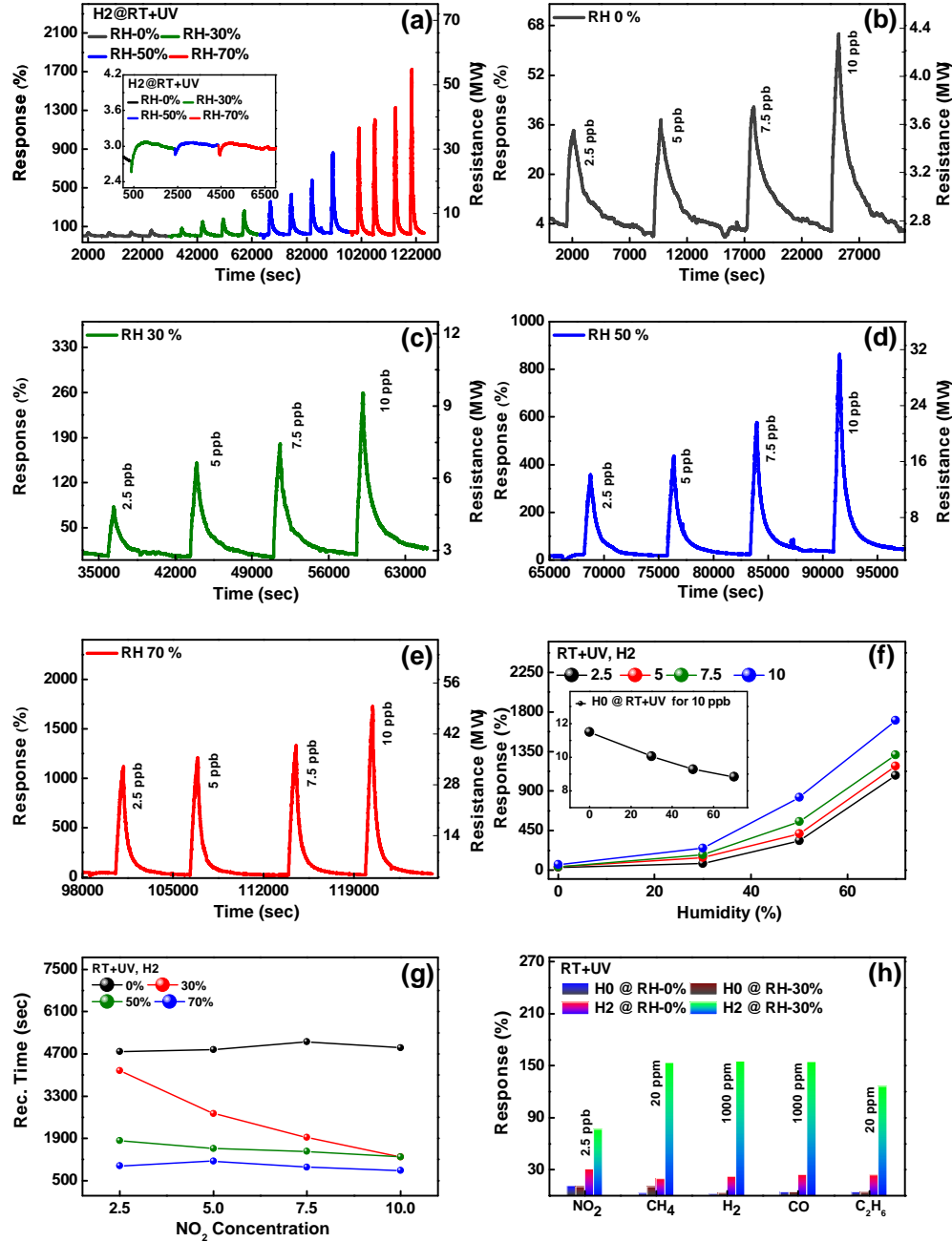


Figure 5: (a) The broad dynamic NO₂ sensing response (2.5 – 10 ppb) at RT under UV illumination obtained from the honeycomb nanomesh device (H2). Inset showed the change in resistance only due to variation in Humidity. The zoomed NO₂ sensing response for different humidity conditions (b) 0% (c) 30% (d) 50% (e) 70%. (f) The summarized sensing response (%) for the honeycomb nanomesh device H2. The inset shows the sensing response (%) for unpatterned device H0. (g) The calculated recovery time for each concentration with variable humidity. The selectivity profile of nanomesh and unpatterned MoS₂ under 0% and 30% RH for various gases under RT with UV illumination.

and red curves denote 0%, 30%, 50%, and 70% humidity, respectively. The inset in Figure 5a shows the change in MoS₂ resistance under the UV light illumination at different humidity levels. It can be seen that the baseline resistance initially drops but quickly recovers (on the period of ~ 20 min). Thus, the effect of humidity is mitigated by the UV illumination with time. The baseline remains stable even under harsh rises in RH, confirming the potential use of MoS₂ nanomeshes for real-world gas sensing applications. Furthermore, Figure 5b-e illustrates a humidity-enhanced NO₂ sensing. Specifically, the response to 2.5 ppb NO₂ is increased 33-fold (from 34% to 1120%) upon RH rise from 0% to 70%. The achieved response values were extremely high for such a low NO₂ concentration with humidity variation, see Figure 5f. They outperform the highest responses at such low NO₂ concentration previously reported for any MoS₂-based sensors (see Figure 6f and Table S1 for detailed comparison). Additionally, the recovery time decreased nearly 6-fold, from 5000 s to 800 s, upon increasing the humidity level, as shown in Figure 5g. We have also tested the unpatterned device H0. These measurements are shown in Figure S7. The inset of Figure 5f shows the NO₂ response under the identical set of humidity conditions for unpatterned device H0, which showed a decreased response with humidity and an overall poor performance. Since the baseline resistance fluctuation is very high due to variation in humidity in this case, we consider the relative response (%) of the signal. The relative response is determined by subtracting the response value when NO₂ is turned on from the response value achieved when NO₂ is off. The baseline resistance was not recovered under UV exposure of unpatterned device H0, unlike the nanomesh device H2, which showed both complete and speed-up recovery. Furthermore, we tested selectivity for various gases under the humid environment (see Figure 5h). We observe improved gas sensing performance for all the studied gases. However, the patterned device H2 exhibits an especially selective and sensitive behavior upon exposure to NO₂. These results further confirm the room temperature, UV-activated, and humidity-enhanced performance of our chemiresistive gas sensor, which paves the way towards real-world gas sensing applications under high humidity conditions.

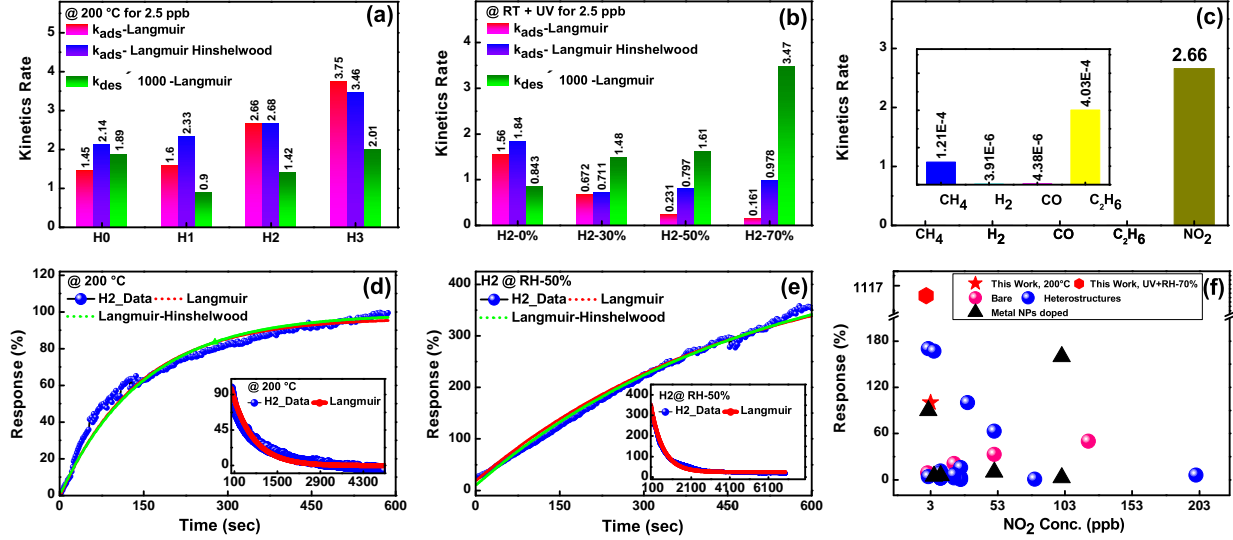


Figure 6: Calculated adsorption rate (k_{ads}) and desorption rate (k_{des}) using the Langmuir and Langmuir-Hinshelwood model for 2.5 ppb NO₂ cycle. The desorption rate (k_{des}) is multiplied by a factor of 1000 for clarity. (a) At $T = 200^\circ\text{C}$. (b) At RT with humidity variation under UV illumination. (c) Fitted adsorption rate (k_{ads}) for different gases. The inset shows the magnified view of four different gases. (d-e) Experimental data fitting for the adsorption profile using Langmuir and L-H model for 2.5 ppb NO₂ cycle for: (d) at $T = 200^\circ\text{C}$ (inset shows the experimental data fitting for the desorption profile), and (e) at RT with 50% humidity under UV illumination. (f) Performance comparison of this work with other relevant publications. The emphasis is given to reports where ppb levels of NO₂ detection has been tested experimentally (see Table S1 for further details)

To understand the role of zigzag edges in honeycomb nanomeshes for NO₂ adsorption, we studied the adsorption and desorption kinetics using the Langmuir and Langmuir-Hinshelwood (L-H) models. We start with discussing the Langmuir model. The adsorption and desorption rate kinetics were calculated for 2.5 ppb NO₂ cycle of each device (H0, H1, H2, and H3) at 200°C and for device H2 only with humidity variation from 0% to 70% using the following two equations.⁵⁶ The desorption kinetics is expressed as:

$$R(t) = R_0 \exp(-k_{des}t), \quad (1)$$

while the adsorption kinetics is:

$$R(t) = R_{\max} \frac{C_a K}{1 + C_a K} \left(1 - \exp \left[- \left(\frac{1 + C_a K}{K} \right) k_{adst} \right] \right). \quad (2)$$

In the above equations, R_{\max} is the maximum response of the sensor for the cycle, R_0 is the response of the sensor during the recovery cycle when NO_2 gas is turned off. k_{ads} and k_{des} are the adsorption and desorption kinetic rates, respectively. K is the adsorption capacity of the sensor, defined as the ratio of k_{ads} and k_{des} , $K = k_{\text{ads}}/k_{\text{des}}$. C_a is the applied NO_2 concentration (2.5 ppb in our calculations). The calculated parameters are depicted in Figure 6a-b. At 200°C , the k_{ads} and k_{des} increase with an increase in the density of hexagons for patterned devices. The higher k_{ads} means stronger interaction of NO_2 gas molecules with the sensing surface. Notably, k_{ads} is 1.86 times higher for honeycomb hexagon device H2 ($2.66 \text{ ppm}^{-1}\text{s}^{-1}$) than the unpatterned device H0 ($1.45 \text{ ppm}^{-1}\text{s}^{-1}$). The enhanced k_{ads} reveals the importance of edges in superior NO_2 gas sensing. Initially, k_{des} is high for the unpatterned device H0; however, it decreases for the honeycomb hexagon device H1, indicating strong adsorption of NO_2 gas molecules in the presence of edges. The value of k_{des} is further increased for devices H2 and H3 due to the higher availability of favorable sites for NO_2 adsorption. The fitting has been performed assuming that NO_2 follows the mass action law, with the response being proportional to the amount of adsorbed NO_2 gas. The desorption energy and charge transfer values of NO_2 on patterned devices may differ from those on unpatterned devices, as suggested by the density functional theory calculations presented below. This can also be inferred from the reduced k_{des} rate when transitioning from device H0 to H1. The patterned devices have similar adsorption and desorption energies but offer a higher number of adsorption sites for NO_2 . Consequently, the k_{des} rate increases further from device H1 to H3.

In Figure 6a, k_{des} for each device have been multiplied by a factor of 1000 for clarity. We note that the Langmuir model fits our experimental findings very well. Therefore, we extended the calculations to NO_2 sensing under variation of humidity and with UV illuminations. However, we observed that k_{ads} rate is decreased with an increase in humidity while k_{des} rate is increased. The calculated k_{des} rate for hexagonal honeycomb device H2 under 70% humidity ($3.47 \times 10^{-3} \text{ s}^{-1}$) is 4.11 times higher than the 0% humidity ($0.84 \times 10^{-3} \text{ s}^{-1}$).

This confirms the improved recovery under humidity with UV illumination. However, at the same time, the k_{ads} rate for hexagonal honeycomb device H2 under 70% humidity (0.16 ppm⁻¹s⁻¹) is 9.68 times lower than the 0% humidity (1.56 ppm⁻¹s⁻¹). The NO₂ response is the highest under 70% RH and with UV illumination which implies that the Langmuir model is not ideal to fit the experimental findings under humidity.

In the Langmuir model, the k_{ads} and k_{des} can be further explained in terms of activation energy at a particular temperature.^{57,58} Furthermore, when the sensor is exposed to light, the adsorption and desorption constants start to depend on the illumination conditions. Additionally, humidity significantly affects the kinetic rates, which needs to be taken into account during the fitting. Hence, a complex interplay between these factors may explain why the Langmuir model does not satisfactorily fit the experimental data under humidity and UV illumination.

To gain further insight into the kinetic processes, we employed the L-H model for 200°C and variable humidity data. The L-H model can be directly obtained from the Langmuir model provided the condition $C_a K \gg 1$ is satisfied (estimated values of $C_a K$ in our case range from 1.5 to 5, depending on the experimental conditions). Thus, the L-H model effectively decouples the desorption process from the adsorption kinetics. With this in mind, the adsorption profile is fitted almost identically by both the L-H and the Langmuir models for devices H0, H1, H2, and H3 at 200°C and device H2 at RT with variation of humidity from 0% to 70% (see Figure 6a,b). The adsorption profile has been fitted using the following equation:⁵⁹

$$R(t) = R_{\text{max}} (1 - e^{-k_{\text{ads}} C_a t}), \quad (3)$$

where, $R(t)$ is the time-dependent response. R_{max} is the maximum response and C_a is the NO₂ concentration (which is 2.5 ppb). The fitted k_{ads} values are displayed on the bar graph in Figure 6a-b. The L-H model adequately fits the experimental data of hexagonal honeycomb device H2 under variable humidity with UV illumination and shows a slight increase in the

adsorption rate with an increase in the hexagon density. This contrasts with the Langmuir model, which in this case showed the opposite trend (see Figure 6b). The experimental data fittings of the adsorption rates using the Langmuir model and L-H model at 200°C and at RT under humidity variation with UV illumination are displayed in Figure 6d-e. The insets of Figure 6d-e additionally show the desorption rates fittings.

To test the specificity of our gas sensors, the adsorption kinetic rates for different gases, including CH₄, H₂, CO, C₄H₆, and NO₂ were obtained using the Langmuir model, see Figure 6c. The corresponding k_{ads} for NO₂ is 2.66 ppm⁻¹s⁻¹, which is at least three orders of magnitude higher than the other measured gases. This confirms the ultra-selective nature of hexagonal honeycomb device H2 for NO₂ gas.

Furthermore, we compared our results with other reports where ppb level NO₂ detection has been tested experimentally. This comparison is displayed in Figure 6f. The comparison has been carried out using certain sensor categories, including bare MoS₂, MoS₂ heterostructure with other materials, and metal nanoparticle doped MoS₂. The corresponding data of response (%), concentration, and temperature from each reference is shown in Table S1. We note that our honeycomb hexagonal sensors, which fall into the category of bare MoS₂ structures, exhibit superior performance compared to other MoS₂-based sensors, even those with more complex configurations like metal nanoparticle doping and heterostructures.

Density function theory calculations

In this section, we complement the measurements with first-principle calculations (see Methods for details) based on density functional theory (DFT) of adsorption energies and charge transfer to an NO₂ molecule adsorbed on MoS₂. These calculations are performed on both the basal plane supercell and the one-dimensional ribbon supercell, considering the three scenarios most relevant to our study. Specifically, we examine NO₂ adsorption on pristine MoS₂, at a sulfur vacancy defect site (S-vacancy site), and at a sulfur vacancy site with an oxygen substitution (O-defect site). The latter two scenarios are particularly pertinent to

our research, as the tested sensing devices are highly susceptible to sulfur vacancy generation due to the fabrication processes, which include both dry and wet chemical etching. Furthermore, these S-vacancy sites are highly prone to oxygen adsorption from the environment. The honeycomb MoS₂ nanomesh can be considered as hexagonal nanoribbons; this is especially clear for thin MoS₂ structures shown in Figure 1b-d. For computational efficiency, we consider only monolayers either in the form of a 5 × 5 supercell or a one-dimensional 6 × 4 ribbon supercell. The structures are shown in Figure 7a,b respectively, where we marked the placement of the defect as the dotted circle. Thus, in total, we consider 9 adsorption geometries. First, these include NO₂ adsorption above the basal plane of a pristine structure, above an S-vacancy and an O-defect. Second, for the MoS₂ ribbon, we consider these three cases next to either of the zigzag edges: the Mo edge (10 $\bar{1}$ 0) terminated with S dimers or a S edge ($\bar{1}$ 010).⁶⁰ An NO₂ molecule was placed next to the marked site and the structure was relaxed using the optPBE-vdW functional until the maximum force on each atom was less than 0.02 eV/Å.

Table 1: Comparison of binding energies ΔE and charge transfer Δq to the adsorbed NO₂ molecule at a particular site on MoS₂: ideal – pristine MoS₂ sheet; S-vac – sulphur vacancy; O-def – oxygen defect; for (top) a 5 × 5 supercell and (bottom) 6 × 4 zigzag ribbon with a Mo edge (10 $\bar{1}$ 0) terminated with S dimers and a S edge ($\bar{1}$ 010).⁶⁰

		5 × 5 monolayer supercell					
		ideal	S-vac	O-def			
ΔE (meV)		-263	-235	-287			
Δq (e)		0.12	0.26	0.11			
		6 × 4 monolayer ribbon					
		Mo edge (10 $\bar{1}$ 0)			S edge ($\bar{1}$ 010)		
		ideal	S-vac	O-def	ideal	S-vac	O-def
ΔE (meV)		-243	-260	-357	-1050	-196	-382
Δq (e)		0.21	0.57	0.31	0.53	0.12	0.26

The final geometries with relaxed NO₂ adsorption are plotted in Figure S8. We focus on two important parameters: adsorption energy and charge transfer. The adsorption energy of each case is calculated as $\Delta E = E_{\text{complex}} - E_{\text{MoS}_2} - E_{\text{NO}_2}$, with negative values indicating

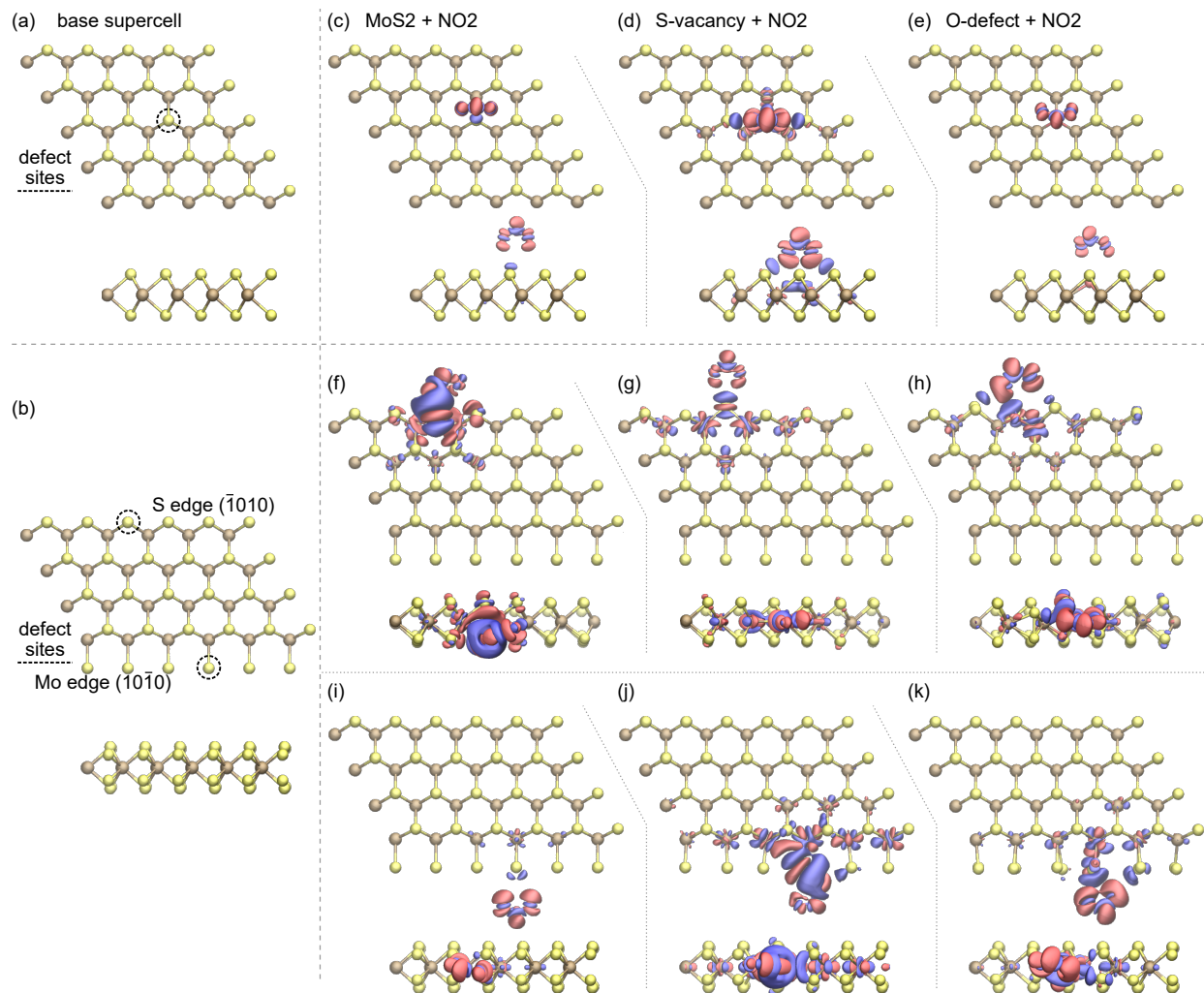


Figure 7: Geometry and electron charge density difference for the considered structures. The pristine MoS₂ structures are sketched in (a) for the 5×5 supercell of MoS₂ monolayer and (b) the 6×4 ribbon supercell. The dashed circles mark the defect placement, though only one defect is present at a time for the ribbon. (c-k) Isosurface plots of the electron charge density difference for NO₂ adsorbed on MoS₂ with top and side views. Charge accumulation is presented in red and depletion in blue.

adsorption is energetically favorable. Here the obtained adsorption energies are static, i.e. at 0 K with the zero point and thermal energies not included, as these have been shown to be small in comparison to the vdW contributions.⁶¹ The energies are reported in Table 1 and all are significantly negative,⁶² indicating efficient adsorption of NO₂ in all cases. We further analyze the charge redistribution in the systems upon NO₂ adsorption based on the Bader charges.⁶³ The positive value indicates that the charge is transferred from MoS₂ to

NO₂. The results confirm that NO₂ plays the role of an acceptor, in every case taking up a sizable amount of charge from MoS₂, as illustrated in Table 1. This charge transfer is also visualized in Figure 7, where charge accumulation can be seen at the position of the NO₂ molecule with an accompanying depletion in the MoS₂. For the ribbon configuration, we analyze both Mo- and S-terminated edges, which are predominantly located at the perimeter of the honeycomb pattern. Consequently, S-vacancy and O-defect sites emerge as the most relevant at the hexagonal perimeter. Our devices were fabricated from a 2H-MoS₂ crystal having AB stacking, which suggests the presence of both types of defect sites in multilayer MoS₂ honeycomb nanomesh structures. This stacking configuration further enhances the potential for diverse defect interactions, contributing to the overall sensing performance. Achieving ideal pristine Mo and S edges and defect-free basal plane supercells is nearly impossible in practical settings due to the inherent limitations of our fabrication processes, which involve both dry and wet etching techniques. Thus, it is likely that in real experiments, the most favorable adsorption sites are S-vacancies and O-defects on one-dimensional edges. The calculated charge transfer is nearly doubled for one-dimensional edges for both Mo- and S-terminated edges in comparison to the basal plane. Moreover, the binding energy is higher for O-defects in all cases.

We now turn our attention to the correlation between the DFT results and our experimental findings. For chemiresistive sensors, charge modulation due to exposed gas molecules is a crucial factor, as it ultimately translates into an electrical signal. A higher charge transfer from MoS₂ to NO₂ results in an enhanced NO₂ sensing response. At room temperature, we find that O-defect sites are predominantly available in the basal plane supercell and in both Mo- and S-terminated ribbon configurations. The combined charge transfer of both edges is substantially higher for the honeycomb MoS₂ nanomesh structure compared to the O-defect sites of the basal plane. Our RT NO₂ sensing experiments conducted without UV activation corroborate this enhanced performance. Specifically, the honeycomb MoS₂ nanomeshes (H2) exhibited nearly doubled NO₂ sensing response compared to the unpat-

terned device (H0), albeit with incomplete recovery. Furthermore, under thermal or UV activation, weakly adsorbed oxygen molecules are desorbed, facilitating NO₂ adsorption at the most favorable sites. Specifically, the S-vacancy and O-defect sites at the edges of honeycomb MoS₂ nanomesh devices exhibit charge transfer values of 0.57*e* and 0.31*e* (at Mo-edge), respectively, making them highly effective for NO₂ sensing.

Discussion of sensing mechanism

In this study, we employed MoS₂ as the active sensing material for the detection of NO₂. MoS₂ nanomeshes were fabricated using flakes mechanically exfoliated from a commercial *n*-type 2H-MoS₂ crystal.⁶⁴ Due to dry and wet etching, the resulting nanomeshes acquire a certain level of *p*-doping, which does not change the overall *n*-type nature of MoS₂. The operational principle underlying the detection of NO₂ involves the perturbation of charge carriers (hence, resistance) in MoS₂ due to the surface charge transfer interactions between the MoS₂ and NO₂ molecules. The NO₂ concentration, flow rate, and the MoS₂ surface stoichiometry influence the sensor's resistance. The interaction between NO₂ and MoS₂ varies under different operating conditions. Therefore, the sensing mechanism involves a complex interplay of physical and chemical processes, making it challenging to define precisely. Given this complexity, a comprehensive understanding of the sensing mechanism requires further investigation beyond the scope of this study. In this section, we briefly summarize the critical aspects of MoS₂ nanomeshes sensing behavior and suggest directions for future research. Detailed discussion is provided in the SI (section "Sensing mechanism").

The oxidative wet etching and environmental factors (gas atmosphere, humidity, temperature, light) significantly alter the MoS₂ surface, potentially capping edges and sulfur vacancies with oxygen molecules or even forming O-defect sites. The nanomesh MoS₂ devices (H1, H2, and H3) feature an abundance of edge sites, possibly capped with oxygen. Enhanced NO₂ adsorption and charge transfer at the MoS₂ edges, particularly in the honeycomb H2, improve device response, affecting resistance even at single-digit ppb NO₂ levels.

In dry air and in the dark, molecular oxygen likely dominates the surfaces of all proposed devices, thereby diminishing the adsorption sites for NO_2 . Despite this, the 2.5 ppb NO_2 response in the patterned device H2 reaches 8%, exceeding the 4% value for the unpatterned device H0. Additionally, the strong binding between NO_2 and MoS_2 leads to incomplete recovery at room temperature in the dark, as illustrated in Figure S9.

To achieve efficient and reversible NO_2 detection, we first raise the temperature to 200°C. NO_2 has higher binding energy to MoS_2 than O_2 , so the elevated temperature facilitates the removal of oxygen adsorbed on the surface and creates more available sites for NO_2 adsorption. At 200°C, MoS_2 nanomeshes show a significantly higher response than the unpatterned device H0, indicating that the edge sites are advantageous for NO_2 sensing. Moreover, the elevated temperature allows for full sensor recovery, which is not possible at room temperature.

In dry air, our second approach leverages UV illumination to both remove the adsorbed oxygen from the surface and enhance NO_2 adsorption. The photogenerated electron-hole pairs are crucial in modulating the adsorption and desorption thermodynamics and kinetics of both O_2 and NO_2 molecules. This effect is especially pronounced in the MoS_2 nanomesh H2, which exhibits higher NO_2 sensitivity than its H0 counterpart. Therefore, UV illumination is critical for amplifying NO_2 detection.

In dark and highly humid environments, the NO_2 sensing mechanism becomes complex, mainly due to the significant influence of water vapor, as elaborated in the SI. The presence of water vapor alters NO_2 detection through interactions with surface-bound hydroxyl ions (OH^-) and protons (H^+). These interactions may lead to the formation of surface-bound nitrate ions ($\text{NO}_3^-(\text{ads})$), which are characterized by their elevated binding energy and enhanced charge transfer on MoS_2 .^{65,66} This process enhances the ability to detect NO_2 in humidity-rich conditions, even in the dark.

The most compelling results of our investigation were achieved under high humidity and UV illumination at RT. Under these conditions, the MoS_2 nanomesh H2 device demonstrated

a universal enhanced sensing response across all tested gases, including NO_2 , CH_4 , H_2 , CO , and C_2H_6 . In contrast, the unpatterned device H0 showed degraded performance when exposed to humidity, highlighting the exceptional role of zigzag edges in the H2 device's enhanced gas sensing capabilities. This universal behavior suggests that the adsorption and charge transfer of all gases is higher in the presence of humidity for MoS_2 nanomesh device H2. Furthermore, it implies that the nanomesh surface has the most available sites for gas molecule adsorption.

While the precise mechanism behind the enhanced sensing performance remains elusive, we hypothesize that the synergy between humidity and UV light optimally cleans the surface. Specifically, UV illumination plays a dual role, removing adsorbed oxygen and preventing the accumulation of surface-bound hydroxyl ions (OH^-) and protons (H^+). This hypothesis is supported by the observed stable baseline resistance even at high RH levels at RT. Therefore, the exceptionally clean surface of our MoS_2 nanomesh H2 device significantly enhances its sensing response across all tested gases. Additionally, we can not rule out the possibility of enhanced adsorption and charge transfer between the exposed gas molecules and MoS_2 nanomesh H2 surface in the presence of adsorbed water. The enhanced NO_2 adsorption and charge transfer in the presence of humidity has been previously reported using DFT.⁶⁷

Conclusion

In conclusion, we have successfully demonstrated the fabrication of controlled, uniform, and sharp zigzag edge enriched hexagons MoS_2 . We developed room-temperature ultra-sensitive, ultra-selective, and humidity-enhanced NO_2 gas sensors. The sensor response to 2.5 ppb NO_2 reaches 99% at $T=200^\circ\text{C}$ and 1120% at room temperature under UV illumination with 70% relative humidity. We showed that honeycomb MoS_2 exhibits superior NO_2 sensing capability due to the high number of zigzag edges, as supported by DFT calculations. Our devices achieved an impressive parts-per-trillion detection limit even at high relative humidity. Our work lays the foundation for developing nanostructured MoS_2 as real-life NO_2

sensors operable at room temperature, under UV light illumination, and in harsh humidity conditions.

METHODS AND MATERIALS

Electrical Contacts Fabrication

The MoS₂ flakes were mechanically exfoliated from HQ-graphene crystals using polydimethylsiloxane (PDMS) stamps and then transferred onto *n*-doped 285 nm SiO₂/Si substrate. The different hexagon devices were fabricated onto identical thickness flakes. The thickness of the flakes was measured using the VEECO profilometer. Finally, the Autocad software was used to design the circular holes and contacts. The flakes with substrates were first covered with a thick layer of 300 nm of 950 PMMA A4 photoresist (MicroChem, USA) using the spin coating technique. The e-beam lithography was employed using the JEOL JBX 9300FS lithographer at 100 kV accelerating voltage and 30 nA current. The lithographically patterned design was developed using 1:3 MIBK:IPA mixture for 2 min and 20 s. The Cr/Au (5/200 nm)metals were evaporated by Lesker PVD 225 e-beam evaporation system (Kurt J. Lesker Company, Germany), followed by overnight liftoff in acetone.

Honeycomb Mesh Nanopatterning

After the device fabrication, we covered the device with a 500 nm thick layer of ARP 6200.13 e-beam resist (Allresist GmbH, Germany). Again, the e-beam lithography was employed using the JEOL JBX 9300FS at 100 kV accelerating voltage and 2 nA current. The lithographically patterned design was developed using *n*-amyl acetate for 1 minute 15 s. The reactive ion etching has been performed in Oxford Plasmalab 100 system (U.K.) using CHF₃ plasma. The dry etching conditions were as follows: CHF₃ and carrier gas (argon) flow were 50 sccm and 40 sccm, respectively. The radio frequency power was 50 W. The MoS₂ etching rate was ~ 10 nm/min. The devices were cleaned using 1165 remover, acetone, and isopropyl alcohol (IPA) for 5 min each. The wet etching process was performed in the mixture

of $\text{H}_2\text{O}_2:\text{NH}_4\text{OH}:\text{H}_2\text{O}$ with a volumetric ratio of 1:1:10 at a slightly elevated temperature.²²

Instrumental Characterization

The SEM imaging was performed using the Ultra 55 FEG SEM at the acceleration voltage of 3 and 4 kV. The Raman spectra were collected at room temperature using the WITEC Alpha 300R equipped with a 532 nm laser with 1800 l/mm grating.

Gas Sensing Experiments

The gas sensing measurements were performed in a home-built sealed chamber, using 20% O_2 and 80% N_2 (dry synthetic air) as the background gas. The source bottle, which was used to produce NO_2 pulses, contained 100 ppb NO_2 in a background of N_2 , with a purity of N6.0. Gas mixing was performed using a gas mixer setup comprising low-flow mass flow controllers (Bronkhorst). The lower NO_2 concentrations were achieved by diluting the original 100 ppb NO_2 using pure N_2 . The overall volume of the sensing environment was always fixed at 100 ml/min. The NO_2 gas was on during measurement for 600 s. The 355 nm UV LED was used for testing the device under UV light. The sensing temperature was controlled using a ceramic heater (Heraeus GmbH, Germany). The electrical testing has been done using the single channel source measure unit (SMU, Keithley 2601 SourceMeter).

DFT calculations

The DFT calculations we carried out using the open-source GPAW package^{68,69} which utilizes the projector-augmented wave method. We used the optPBE-vdW functional to treat the exchange-correlation potential and van der Waals interactions.⁷⁰ For the basal plane calculations, we used a $5 \times 5 \times 1$ supercell of 1H-MoS₂ with 15 Å of vacuum above and below the monolayer to avoid interlayer interactions. The Kohn-Sham orbitals were expanded using a plane wave basis set with an energy cutoff of 500 eV, we used a $5 \times 5 \times 1$ Monkhorst-Pack grid for the \mathbf{k} -mesh and a grid spacing of less than 0.2 Å. The MoS₂ ribbon was constructed from

a pristine 6×5 monolayer by removing the first row of Mo atoms, leaving an S-terminated ribbon on both sides. The vacuum for the ribbon was set to 10 \AA above and below, as well as to either side of the edges. For these calculations, we used a $5 \times 1 \times 1$ Monkhorst-Pack grid for the \mathbf{k} -mesh, while the other parameters were the same. For all calculations, we used Fermi-Dirac occupation number smearing with a factor of 20 meV and line-shape broadening of 50 meV.

Initially, we relaxed the pristine 5×5 monolayer and the 6×4 ribbon until the maximum force on each atom was smaller than 5 meV/\AA . Next, the relaxed structures were modified by introducing the two types of defects. These structures were subsequently relaxed using the same conditions. The final relaxed structures (with and without defects) had NO_2 added to the vicinity of the defect (or, respectively, where it would be) and relaxed until the forces were less than 0.02 eV/\AA .

Supporting Information Available

Detailed experimental procedures, supplementary notes, and additional characterization data.

Acknowledgement

This work was performed in part at Myfab Chalmers and Chalmers Materials Analysis Laboratory (CMAL). A.V.A. is thankful to SIO Grafen's 2D Graduate network for the mobility grant to conduct experiments at Linköping University. A.V.A, A.Yu.P, and T.O.S. acknowledge funding from the Olle Engkvist Foundation (Grant No. 211-0063), 2D-TECH VINNOVA competence center (Ref. 2019-00068), Chalmers Excellence Initiative Nano, and Knut and Alice Wallenberg Foundation (KAW, grant No. 2019.0140). T.J.A. acknowledges funding from the Polish National Science Center, project 2019/34/E/ST3/00359.

Conflicts of interest

The authors declare no conflicts of interest.

Keywords

nitrogen dioxide (NO₂) gas sensing, nanostructured molybdenum disulfide (MoS₂), transition metal dichalcogenides, relative humidity, chemiresistive gas sensing

References

1. Atkinson, R. Atmospheric chemistry of VOCs and NO_x. *Atmospheric environment* **2000**, *34*, 2063–2101.
2. Vineis, P.; Forastiere, F.; Hoek, G.; Lipsett, M. Outdoor air pollution and lung cancer: recent epidemiologic evidence. *Int. J. Cancer* **2004**, *111*, 647–652.
3. Schwela, D. Air pollution and health in urban areas. *Reviews on environmental health* **2000**, *15*, 13–42.
4. Hodge, C. A. *Pollution control in fertilizer production*; CRC Press, 1994.
5. Korn, S.; Wilk, M.; Voigt, S.; Weber, S.; Keller, T.; Buhl, R. Measurement of fractional exhaled nitric oxide: comparison of three different analysers. *Respiration* **2020**, *99*, 1–8.
6. Esworthy, R.; McCarthy, J. E. The National Ambient Air Quality Standards (NAAQS) for Particulate Matter (PM): EPA’s 2006 Revisions and Associated Issues. 2013.
7. Guarnieri, M.; Balmes, J. R. Outdoor air pollution and asthma. *The Lancet* **2014**, *383*, 1581–1592.
8. Splendiani, A.; Sun, L.; Zhang, Y.; Li, T.; Kim, J.; Chim, C.-Y.; Galli, G.; Wang, F. Emerging photoluminescence in monolayer MoS₂. *Nano Lett.* **2010**, *10*, 1271–1275.
9. Radisavljevic, B.; Radenovic, A.; Brivio, J.; Giacometti, V.; Kis, A. Single-layer MoS₂ transistors. *Nat. Nanotechnol.* **2011**, *6*, 147–150.
10. Jaramillo, T. F.; Jørgensen, K. P.; Bonde, J.; Nielsen, J. H.; Horch, S.; Chorkendorff, I. Identification of active edge sites for electrochemical H₂ evolution from MoS₂ nanocatalysts. *Science* **2007**, *317*, 100–102.
11. Yue, Q.; Shao, Z.; Chang, S.; Li, J. Adsorption of gas molecules on monolayer MoS₂ and effect of applied electric field. *Nanoscale Res. Lett.* **2013**, *8*, 1–7.

12. Cho, S.-Y.; Kim, S. J.; Lee, Y.; Kim, J.-S.; Jung, W.-B.; Yoo, H.-W.; Kim, J.; Jung, H.-T. Highly enhanced gas adsorption properties in vertically aligned MoS₂ layers. *ACS Nano* **2015**, *9*, 9314–9321.
13. Agrawal, A. V.; Kumar, R.; Venkatesan, S.; Zakhidov, A.; Yang, G.; Bao, J.; Kumar, M.; Kumar, M. Photoactivated mixed in-plane and edge-enriched *p*-type MoS₂ flake-based NO₂ sensor working at room temperature. *ACS Sensors* **2018**, *3*, 998–1004.
14. Kim, T.; Lee, T. H.; Park, S. Y.; Eom, T. H.; Cho, I.; Kim, Y.; Kim, C.; Lee, S. A.; Choi, M.-J.; Suh, J. M.; others Drastic Gas Sensing Selectivity in 2-Dimensional MoS₂ Nanoflakes by Noble Metal Decoration. *ACS Nano* **2023**, *17*, 4404–4413.
15. Long, H.; Harley-Trochimczyk, A.; Pham, T.; Tang, Z.; Shi, T.; Zettl, A.; Carraro, C.; Worsley, M. A.; Maboudian, R. High surface area MoS₂/graphene hybrid aerogel for ultrasensitive NO₂ detection. *Adv. Func. Mater.* **2016**, *26*, 5158–5165.
16. Shim, J.; Sen, A.; Park, K.; Park, H.; Bala, A.; Choi, H.; Park, M.; Kwon, J. Y.; Kim, S. Nanoporous MoS₂ Field-Effect Transistor Based Artificial Olfaction: Achieving Enhanced Volatile Organic Compound Detection Inspired by the Drosophila Olfactory System. *ACS Nano* **2023**, *17*, 21719–21729.
17. Bala, A.; Sen, A.; Kim, Y.-H.; Kim, Y.-M.; Gandla, S.; Park, H.; Kim, S. Large-Area MoS₂ Nanosheets with Triangular Nanopore Arrays as Active and Robust Electrocatalysts for Hydrogen Evolution. *J. Phys. Chem. C* **2022**, *126*, 9696–9703.
18. Sen, A.; Shim, J.; Bala, A.; Park, H.; Kim, S. Boosting Sensitivity and Reliability in Field-Effect Transistor-Based Biosensors with Nanoporous MoS₂ Encapsulated by Non-Planar Al₂O₃. *Adv. Funct. Mater.* **2023**, *33*, 2301919.
19. Park, H.; Lee, J.; Han, G.; AlMutairi, A.; Kim, Y.-H.; Lee, J.; Kim, Y.-M.; Kim, Y. J.; Yoon, Y.; Kim, S. Nano-patterning on multilayer MoS₂ via block copolymer lithography for highly sensitive and responsive phototransistors. *Commun. Mater.* **2021**, *2*, 94.

20. Munkhbat, B.; Küçüköz, B.; Baranov, D. G.; Antosiewicz, T. J.; Shegai, T. O. Nanostructured transition metal dichalcogenide multilayers for advanced nanophotonics. *Laser & Photonics Rev.* **2023**, *17*, 2200057.
21. Xiao, S.-L.; Yu, W.-Z.; Gao, S.-P. Edge preference and band gap characters of MoS₂ and WS₂ nanoribbons. *Surf. Sci.* **2016**, *653*, 107–112.
22. Munkhbat, B.; Yankovich, A. B.; Baranov, D. G.; Verre, R.; Olsson, E.; Shegai, T. O. Transition metal dichalcogenide metamaterials with atomic precision. *Nat. Commun.* **2020**, *11*, 4604.
23. Jessen, B. S.; Gammelgaard, L.; Thomsen, M. R.; Mackenzie, D. M.; Thomsen, J. D.; Caridad, J. M.; Duegaard, E.; Watanabe, K.; Taniguchi, T.; Booth, T. J.; others Lithographic band structure engineering of graphene. *Nat. Nanotechnol.* **2019**, *14*, 340–346.
24. Liu, M.; Huang, Z.; Guo, Y.; Zhang, Z.; Zhang, L.; Zhang, H.; Zhong, J.; Li, S.; Deng, W.; Wang, D.; others Patterning two-dimensional semiconductors with thermal etching. *InfoMat* **2023**, *5*, e12474.
25. Cao, L.; Yang, S.; Gao, W.; Liu, Z.; Gong, Y.; Ma, L.; Shi, G.; Lei, S.; Zhang, Y.; Zhang, S.; others Direct laser-patterned micro-supercapacitors from paintable MoS₂ films. *Small* **2013**, *9*, 2905–2910.
26. Enrico, A.; Hartwig, O.; Dominik, N.; Quellmalz, A.; Gylfason, K. B.; Duesberg, G. S.; Niklaus, F.; Stemme, G. Ultrafast and Resist-Free Nanopatterning of 2D Materials by Femtosecond Laser Irradiation. *ACS Nano* **2023**, *17*, 8041–8052.
27. Chang, S.; Yan, Y.; Geng, Y. Manipulating Nanopatterns on Two-Dimensional MoS₂ Monolayers via Atomic Force Microscopy-Based Thermomechanical Nanolithography for Optoelectronic Device Fabrication. *ACS Appl. Nano Mater.* **2023**, *6*, 8346–8357.

28. Way, A. J.; Jacobberger, R. M.; Arnold, M. S. Seed-initiated anisotropic growth of unidirectional armchair graphene nanoribbon arrays on germanium. *Nano Lett.* **2018**, *18*, 898–906.
29. Yu, Q.; Jauregui, L. A.; Wu, W.; Colby, R.; Tian, J.; Su, Z.; Cao, H.; Liu, Z.; Pandey, D.; Wei, D.; Fung Chung, T.; Peng, P.; Guisinger, N. P.; Stach, E. A.; Bao, J.; Pei, S.-S.; Chen, Y. P. Control and characterization of individual grains and grain boundaries in graphene grown by chemical vapour deposition. *Nat. Mater.* **2011**, *10*, 443–449.
30. Li, Y.; Hao, S.; DiStefano, J. G.; Murthy, A. A.; Hanson, E. D.; Xu, Y.; Wolverton, C.; Chen, X.; Dravid, V. P. Site-specific positioning and patterning of MoS₂ monolayers: The role of Au seeding. *ACS Nano* **2018**, *12*, 8970–8976.
31. Ryu Cho, Y. K.; Rawlings, C. D.; Wolf, H.; Spieser, M.; Bisig, S.; Reidt, S.; Sousa, M.; Khanal, S. R.; Jacobs, T. D.; Knoll, A. W. Sub-10 nanometer feature size in silicon using thermal scanning probe lithography. *ACS Nano* **2017**, *11*, 11890–11897.
32. Liu, X.; Howell, S. T.; Conde-Rubio, A.; Boero, G.; Brugger, J. Thermomechanical nanocutting of 2D materials. *Adv. Mater.* **2020**, *32*, 2001232.
33. Yoon, J.-W.; Kim, J.-S.; Kim, T.-H.; Hong, Y. J.; Kang, Y. C.; Lee, J.-H. A new strategy for humidity independent oxide chemiresistors: dynamic self-refreshing of In₂O₃ sensing surface assisted by layer-by-layer coated CeO₂ nanoclusters. *Small* **2016**, *12*, 4229–4240.
34. Reddeppa, M.; Park, B.-G.; Murali, G.; Choi, S. H.; Chinh, N. D.; Kim, D.; Yang, W.; Kim, M.-D. NO_x gas sensors based on layer-transferred *n*-MoS₂/*p*-GaN heterojunction at room temperature: study of UV light illuminations and humidity. *Sensors and Actuators B: Chemical* **2020**, *308*, 127700.
35. Wang, J.; Shen, Y.; Li, X.; Xia, Y.; Yang, C. Synergistic effects of UV activation and surface oxygen vacancies on the room-temperature NO₂ gas sensing performance of ZnO nanowires. *Sensors and Actuators B: Chemical* **2019**, *298*, 126858.

36. Chen, X.; Hu, J.; Chen, P.; Yin, M.; Meng, F.; Zhang, Y. UV-light-assisted NO₂ gas sensor based on WS₂/PbS heterostructures with full recoverability and reliable anti-humidity ability. *Sensors and Actuators B: Chemical* **2021**, *339*, 129902.
37. Ma, N.; Suematsu, K.; Yuasa, M.; Shimano, K. Pd size effect on the gas sensing properties of Pd-loaded SnO₂ in humid atmosphere. *ACS Appl. Mater. Int.* **2015**, *7*, 15618–15625.
38. Wang, L.; Lou, Z.; Fei, T.; Zhang, T. Templating synthesis of ZnO hollow nanospheres loaded with Au nanoparticles and their enhanced gas sensing properties. *J. Mater. Chem.* **2012**, *22*, 4767–4771.
39. Yang, M.; Lu, J.; Wang, X.; Zhang, H.; Chen, F.; Sun, J.; Yang, J.; Sun, Y.; Lu, G. Acetone sensors with high stability to humidity changes based on Ru-doped NiO flower-like microspheres. *Sensors and Actuators B: Chemical* **2020**, *313*, 127965.
40. Qin, Y.; Zang, J.; Bai, C.; Wang, X. Dual functionalization of aligned silicon nanowires by APTES and nano-Ag to achieve high response to rarefied acetone at high ambient humidity. *J. Mater. Sci.: Materials in Electronics* **2021**, *32*, 908–922.
41. Kim, J.-S.; Na, C. W.; Kwak, C.-H.; Li, H.-Y.; Yoon, J. W.; Kim, J.-H.; Jeong, S.-Y.; Lee, J.-H. Humidity-independent gas sensors using Pr-doped In₂O₃ macroporous spheres: role of cyclic Pr³⁺/Pr⁴⁺ redox reactions in suppression of water-poisoning effect. *ACS Appl. Mater. Int.* **2019**, *11*, 25322–25329.
42. Li, X.; Zhang, L.; Yang, Z.; He, Z.; Wang, P.; Yan, Y.; Ran, J. Hydrophobic modified activated carbon using PDMS for the adsorption of VOCs in humid condition. *Separation and Purification Technology* **2020**, *239*, 116517.
43. Maity, D.; Kumar, R. T. R. Polyaniline anchored MWCNTs on fabric for high performance wearable ammonia sensor. *ACS Sensors* **2018**, *3*, 1822–1830.

44. Iqbal, M. W.; Shahzad, K.; Akbar, R.; Hussain, G. A review on Raman finger prints of doping and strain effect in TMDCs. *Microelectronic Engineering* **2020**, *219*, 111152.
45. Chakraborty, B.; Bera, A.; Muthu, D.; Bhowmick, S.; Waghmare, U. V.; Sood, A. Symmetry-dependent phonon renormalization in monolayer MoS₂ transistor. *Phys. Rev. B* **2012**, *85*, 161403.
46. Kong, D.; Wang, H.; Cha, J. J.; Pasta, M.; Koski, K. J.; Yao, J.; Cui, Y. Synthesis of MoS₂ and MoSe₂ films with vertically aligned layers. *Nano Lett.* **2013**, *13*, 1341–1347.
47. Kim, T.; Kim, D.; Choi, C. H.; Joung, D.; Park, J.; Shin, J. C.; Kang, S.-W. Structural defects in a nanomesh of bulk MoS₂ using an anodic aluminum oxide template for photoluminescence efficiency enhancement. *Sci. Rep.* **2018**, *8*, 6648.
48. Lee, C.; Yan, H.; Brus, L. E.; Heinz, T. F.; Hone, J.; Ryu, S. Anomalous lattice vibrations of single- and few-layer MoS₂. *ACS Nano* **2010**, *4*, 2695–2700.
49. Agrawal, A. V.; Kumar, N.; Kumar, M. Strategy and future prospects to develop room-temperature-recoverable NO₂ gas sensor based on two-dimensional molybdenum disulfide. *Nano-micro Lett.* **2021**, *13*, 1–58.
50. David, S. S.; Veeralakshmi, S.; Nehru, S.; Kalaiselvam, S. A highly sensitive, selective and room temperature operatable formaldehyde gas sensor using chemiresistive g-C₃N₄/ZnO. *Mater. Adv.* **2020**, *1*, 2781–2788.
51. Pei, Y.; Zhang, X.; Hui, Z.; Zhou, J.; Huang, X.; Sun, G.; Huang, W. Ti₃C₂T_X MXene for sensing applications: recent progress, design principles, and future perspectives. *ACS Nano* **2021**, *15*, 3996–4017.
52. Borini, S.; White, R.; Wei, D.; Astley, M.; Haque, S.; Spigone, E.; Harris, N.; Kivioja, J.; Ryhänen, T. Ultrafast graphene oxide humidity sensors. *ACS Nano* **2013**, *7*, 11166–11173.

53. Potyrailo, R. A.; Surman, C.; Nagraj, N.; Burns, A. Materials and transducers toward selective wireless gas sensing. *Chem. Rev.* **2011**, *111*, 7315–7354.
54. Chen, R. J.; Franklin, N. R.; Kong, J.; Cao, J.; Tomblor, T. W.; Zhang, Y.; Dai, H. Molecular photodesorption from single-walled carbon nanotubes. *Appl. Phys. Lett.* **2001**, *79*, 2258–2260.
55. Zhang, L.; Li, Z.; Liu, J.; Peng, Z.; Zhou, J.; Zhang, H.; Li, Y. Optoelectronic gas sensor based on few-layered InSe nanosheets for NO₂ detection with ultrahigh antihumidity ability. *Anal. Chem.* **2020**, *92*, 11277–11287.
56. Koo, W.-T.; Kim, S.-J.; Jang, J.-S.; Kim, D.-H.; Kim, I.-D. Catalytic metal nanoparticles embedded in conductive metal–organic frameworks for chemiresistors: highly active and conductive porous materials. *Adv. Sci.* **2019**, *6*, 1900250.
57. Zhang, C.; Boudiba, A.; De Marco, P.; Snyders, R.; Olivier, M.-G.; Debligny, M. Room temperature responses of visible-light illuminated WO₃ sensors to NO₂ in sub-ppm range. *Sensors and Actuators B: Chemical* **2013**, *181*, 395–401.
58. Gu, D.; Wang, X.; Liu, W.; Li, X.; Lin, S.; Wang, J.; Rumyantseva, M. N.; Gaskov, A. M.; Akbar, S. A. Visible-light activated room temperature NO₂ sensing of SnS₂ nanosheets based chemiresistive sensors. *Sensors and Actuators B: Chemical* **2020**, *305*, 127455.
59. Lee, C. Y.; Strano, M. S. Understanding the dynamics of signal transduction for adsorption of gases and vapors on carbon nanotube sensors. *Langmuir* **2005**, *21*, 5192–5196.
60. Bollinger, M. V.; Lauritsen, J. V.; Jacobsen, K. W.; Nørskov, J. K.; Helveg, S.; Besenbacher, F. One-Dimensional Metallic Edge States in MoS₂. *Phys. Rev. Lett.* **2001**, *87*, 196803.
61. Rana, M. K.; Koh, H. S.; Hwang, J.; Siegel, D. J. Comparing van der Waals density

- functionals for CO₂ adsorption in metal organic frameworks. *J. Phys. Chem. C* **2012**, *116*, 16957–16968.
62. Zhao, S.; Xue, J.; Kang, W. Fas absorption on MoS₂ monolayer from first-principles calculations. *Chem. Phys. Lett.* **2014**, *595-596*, 35–42.
63. Tang, W.; Sanviller, E.; Henkelman, G. A grid-based Bader analysis algorithm without lattice bias. *J. Phys.: Condens. Matter* **2009**, *21*, 084204.
64. MoS₂ – Molybdenum Disulfide. <https://www.hqgraphene.com/MoS2.php>.
65. Yao, F.; Duong, D. L.; Lim, S. C.; Yang, S. B.; Hwang, H. R.; Yu, W. J.; Lee, I. H.; Güneş, F.; Lee, Y. H. Humidity-assisted selective reactivity between NO₂ and SO₂ gas on carbon nanotubes. *J. Mater. Chem.* **2011**, *21*, 4502–4508.
66. Han, Y.; Liu, Y.; Su, C.; Wang, S.; Li, H.; Zeng, M.; Hu, N.; Su, Y.; Zhou, Z.; Wei, H.; others Interface engineered WS₂/ZnS heterostructures for sensitive and reversible NO₂ room temperature sensing. *Sensors and Actuators B: Chemical* **2019**, *296*, 126666.
67. Azizi, A.; Dogan, M.; Long, H.; Cain, J. D.; Lee, K.; Eskandari, R.; Varieschi, A.; Glazer, E. C.; Cohen, M. L.; Zettl, A. High-performance atomically-thin room-temperature NO₂ sensor. *Nano Lett.* **2020**, *20*, 6120–6127.
68. Mortensen, J.; Hansen, L.; Jacobsen, K. Real-space grid implementation of the projector augmented wave method. *Phys. Rev. B* **2005**, *71*, 035109.
69. Enkovaara, J.; Rostgaard, C.; Mortensen, J.; Chen, J.; Dulak, M.; Ferrighi, L.; an C. Glinsvad, J. G.; Haikola, V.; Hansen, H.; Kristoffersen, H.; Kuisma, M.; Larsen, A.; Lehtovaara, L.; Ljungberg, M.; Lopez-Acevedo, O.; Moses, P.; Ojanen, J.; Olsen, T.; Petzold, V.; Romero, N. *et al.* Electronic structure calculations with GPAW: a real-space implementation of the projector augmented-wave method. *J. Phys.: Condens. Matter* **2010**, *22*, 253202.

70. Larsen, A. H.; Kuisma, M.; Löfgren, J.; Pouillon, Y.; Erhart, P.; Hyldgaard, P. libvdwxc: a library for exchange–correlation functionals in the vdW-DF family. *Modelling Simul. Mater. Sci. Eng.* **2017**, *25*, 065004.

TOC Graphic

